
PILOT TONE-GUIDED FOCUSED NAVIGATION FOR FREE-BREATHING WHOLE-LIVER FAT-WATER AND T2* QUANTIFICATION

Adèle LC Mackowiak^{1,2,3}, Christopher W Roy¹, Mariana BL Falcão¹, Mario Bacher^{1,6}, Aurélien Bustin^{1,4,5}, Jérôme Yerly^{1,7}, Peter Speier⁶, Matthias Stuber^{1,7}, Naïk Vietti-Violi¹, Jessica AM Bastiaansen^{2,3}

¹Department of Radiology, Lausanne University Hospital (CHUV) and University of Lausanne (UNIL), Lausanne, Switzerland

²Department of Diagnostic, Interventional and Pediatric Radiology (DIPR), Inselspital, Bern University Hospital, University of Bern, Switzerland

³Translational Imaging Center (TIC), Swiss Institute for Translational and Entrepreneurial Medicine, Bern, Switzerland

⁴Department of Cardiovascular Imaging, Hôpital Cardiologique du Haut-Lévêque, CHU de Bordeaux, France

⁵IHU LIRYC, Electrophysiology and Heart Modelling Institute, INSERM U1045, Centre de Recherche Cardio-Thoracique de Bordeaux, France

⁶Siemens Healthcare GmbH, Erlangen, Germany

⁷CIBM Center for Biomedical Imaging, Lausanne, Switzerland

Corresponding author: Jessica A.M. Bastiaansen, Ph.D., Assist. Prof.

Email: jbastiaansen.mri@gmail.com

Freiburgstrasse 3, 3010 Bern, Switzerland. Department of Diagnostic, Interventional and Pediatric Radiology (DIPR), Inselspital, Bern University Hospital, University of Bern, Switzerland

Manuscript type: Technical Note (Max 2800 words, 5 objects (figures + tables))

Word count:

Abstract: 250

Total Body: 2782

Introduction: 461

Methods: 956

Results: 790

Discussion: 575

ABSTRACT

Purpose

To achieve whole-liver motion-corrected fat fraction (FF) and $R2^*$ quantification with a 3-minute free-breathing (FB) 3D radial isotropic acquisition, for increased organ coverage, ease-of-use, and patient comfort.

Methods

A FB 3D radial multiecho gradient-echo liver acquisition with integrated Pilot Tone (PT) navigation and $N_{TE}=8$ echoes was reconstructed with a motion-correction algorithm based on focused navigation and guided by PT signals (PT-fNAV), with and without a denoising step. Fat fraction (FF) and $R2^*$ quantification using a graph cut algorithm was performed on the motion-corrected whole-liver multiecho volumes. Volunteer experiments ($n=10$) at 1.5T included reference 3D and 2D Cartesian breath-hold (BH) acquisitions. Image sharpness was assessed to evaluate the quality of motion correction with PT-fNAV, compared to a motion-resolved reconstruction. Fat-water images and parametric maps were compared to BH reference acquisitions following Cartesian trajectories, and to a routinely used clinical software (MRQuantif).

Results

The image sharpness provided by PT-fNAV (with and without denoising) was similar in end-expiratory motion-resolved reconstructions. The 3D radial FB FF maps compared well with reference BH 3D Cartesian maps (bias +0.7%, limits of agreement (LOA) [-2.5; 4.0]%) and with 2D quantification with MRQuantif (-0.2%, LOA [-1.1; 0.6]%). While expected visual deviations between proposed FB and reference BH $R2^*$ maps were observed, no significant differences were found in quantitative analyses.

Conclusion

A 3D radial technique with retrospective motion correction by PT-fNAV enabled FF and $R2^*$ quantification of the whole-liver at 1.5T. The FB whole-liver acquisition at isotropic spatial resolution compared in accuracy with BH techniques, enabling 3D assessment of steatosis in individuals with limited respiratory capabilities.

INTRODUCTION

The incidence of fatty liver diseases is rapidly increasing worldwide¹, particularly in the context of the obesity epidemic². Chemical shift-encoded MRI (CSE-MRI) enables the noninvasive quantification of fat³⁻⁵, providing an accurate alternative to gold-standard liver biopsies⁶⁻⁹, which is crucial for monitoring the treatment of hepatic steatosis^{10,11}. CSE-MRI is typically performed with multiecho gradient-echo (ME-GRE) sequences, requiring the acquisition of a large number of echoes to resolve the fat spectrum in its entirety^{3,12} and to quantify $R2^*$ ¹³, which is a metric for excessive iron deposition¹⁴. Unlike focal biopsies, CSE-MRI is not limited in organ coverage and can account for steatosis heterogeneity^{15,16}.

Traditional CSE-MRI uses Cartesian sampling and breath-hold (BH) techniques, which are sensitive to physiological motion and can be challenging due to patient compliance. The volumetric interpolated BH examination (VIBE) technique¹⁷⁻¹⁹ necessitates multiple slices for whole-organ coverage, leading to repeated BH or long scans. Free-breathing (FB) techniques increase ease-of-use, scanning efficiency, and patient comfort, making them particularly beneficial for populations where BHs are not sustainable. Additionally, FB techniques enable accurate quantitative imaging²⁰⁻²³, which often requires longer scan times.

In contrast to Cartesian sampling, CSE-MRI using radial k-space trajectories is inherently robust to motion, which can often be extracted from the data itself²⁴. Advanced motion-resolved approaches using compressed sensing²⁵⁻²⁷ (CS), or self-gating (SG) approaches in multiecho GRE acquisitions^{21,28-31}, have surpassed the motion averaging methods initially employed^{27,32,33}. Nevertheless, the parametric maps obtained with the aforementioned studies focused on 1-dimensional translational motion of the liver, potentially neglecting the more complex respiratory motion patterns of the organ.

Recently, a focused navigation (fNAV) algorithm was introduced³⁴, based on autofocusing^{35,36}, which extracts 3D displacement fields of both rigid and non-rigid motion. fNAV abbreviated reconstruction time in comparison to CS techniques when applied to the heart^{34,37}. In parallel, 3D radial golden-angle trajectories facilitated highly under-sampled FB ME-GRE acquisitions, allowing for isotropic fat-water quantification in large volumes³⁸. In this prior study³⁸, improved motion correction was achieved when combined with Pilot Tone³⁹ (PT) navigation, which can benefit low SNR sequences like GRE. Therefore, it is hypothesized that by leveraging a 3D radial trajectory, a non-rigid motion-correction algorithm, and PT navigation, whole-liver quantification of FF and R2* of similar accuracy to BH reference scans can be obtained under free-breathing conditions.

The goal of the study was to address the need for whole-liver free-breathing quantitative imaging, by applying PT-guided fNAV reconstruction to 3D radial FB ME-GRE acquisitions. Whole-liver FF and R2* quantification was performed in volunteers at 1.5T. The impact of motion correction with PT-fNAV on parametric mapping, and the agreement of 3D radial FB motion-corrected images and maps with reference BH Cartesian acquisitions, were determined. A comparison with FF and R2* estimates from a routinely used MRQuantIF clinical software for iron and fat quantification was provided.

METHODS

2.1. MRI experiments

Ten healthy subjects enrolled in the study (F=6, median age [\pm interquartile range]: 26.5 [\pm 3.25] y.o., body mass index: 22.7 [\pm 3.4]) after consent was collected following institutional rules (authorization CER-VD 2021-007008 Switzerland). Experiments were performed on a 1.5T clinical scanner (MAGNETOM Sola, Siemens Healthcare, Erlangen, Germany) using a 12-

channel body array with a PT generator (Biomatrix Body 12, Siemens Healthcare, Erlangen, Germany). A free-breathing 3D radial ME-GRE sequence³⁸ with $N_{TE}=8$ echoes was used. The spiral phyllotaxis⁴⁰ trajectory used consisted of 424 interleaved spirals of 22 readout lines each, resulting in a dataset under-sampled to 16% of the Nyquist criterion, corresponding to an acceleration factor $R=6.21$ and leading to a fixed scan time $TA=2:57min$ in all subjects. Reference acquisitions included a 3D ME-GRE scan with 8 slices (3D Cartesian BH), a 2D 2-point Dixon VIBE scan (2D Cartesian 2p-Dixon VIBE BH), and a 2D ME-GRE scan with $N_{TE}=10$ echoes (2D MRQuantif BH, recommended protocol for processing with MRQuantif software, see <https://imagedmed.univ-rennes1.fr/en/mrquantif/overview>), all acquired with a 5mm slice thickness in a single BH. Sequence parameters are detailed in **Table 1**.

All the BH protocols were performed either at end-expiration ($n=6/10$) or end-inspiration according to the subject's capability. Images from the reference breath-held scans (3D Cartesian BH, 2D 2p-Dixon VIBE BH, and 2D MRQuantif BH) were reconstructed at the scanner using built-in vendor software.

Sequence parameters	3D radial FB	3D Cartesian BH	2D Cartesian 2p-Dixon VIBE BH	2D MRQuantif BH
Respiratory condition	Free breathing	Breath hold	Breath hold	Breath hold
FOV size [mm²]	290*290	290*290	290*290	290*290
FOV phase [%]	100	87.5	81.3	87.5
Spatial resolution [mm³]	1.5*1.5*1.5	1.5*1.5*5.0	1.5*1.5*5.0	1.5*1.5*5.0
Number of slices	192	8	8	3
Slab coverage [cm]	28.8	4	4	1.5
Readout trajectory	phyllotaxis ⁴⁰	Cartesian	Cartesian	Cartesian
TR [ms]	19.02	19.24	6.70	120.00
$\Delta TE/TE_1$ [ms]	2.30/1.38	2.30/1.30	2.38/2.39	2.38/2.38
Number of echoes N_{TE}	8	8	2	10
Flip angle [°]	12	12	10	20

Pixel bandwidth [Hz/px]	898	898	470	530
Gradient readout mode	monopolar	monopolar	bipolar	bipolar
Acceleration factor R	6.2 (fNAV) 24.8 (motion-resolved)	none	4	none
TA [min]	02:57	00:20	00:07	00:15

Table 1 Sequence parameters for MRI volunteer experiments at 1.5T.

Abbreviations: BH, breath-hold; fNAV, focused navigation; FOV, field-of-view; FB, free-breathing; TA, acquisition time; TE, echo time; TR, repetition time.

2.2. 3D radial free-breathing image reconstruction

All reconstruction steps were performed in MATLAB R2021b (The Mathworks, Natick, MA, USA). A 1D respiratory signal trace was extracted⁴¹ from the PT signals sampled at a 2kHz rate throughout the acquisition (**Figure 1**). The end-expiratory position in PT signals was identified and chosen to guide all fNAV reconstructions. Respiration was also measured by a respiratory sensor (RSR) built into the scanner, as a reference. The fNAV iterative reconstruction used a non-uniform FFT and coil sensitivity profiles. At each iteration, 3D amplitude coefficients $\mathbf{A}(\mathbf{r})$ are computed at each location \mathbf{r} and updated following a metric of gradient entropy³⁵ for image blur assessment. The initial coefficients were restricted to rigid displacements in a selected ROI, and non-rigid motion was modeled afterwards as a sum of rigid displacements. The final corrected volumes are obtained when both the entropy metric converges to a minimum and a smoothness constraint applied on the displacement field is optimized.

The correction coefficients determined with fNAV were applied to each set of echoes, and 3D coil sensitivities were computed using data from the first echo. Following fNAV reconstruction, the motion-corrected multiecho volumes were denoised using multi-contrast

patch-based denoising⁴², with a regularization coefficient of $\sigma=75$ and a patch size of 9x9 pixels. Computation times were recorded.

To evaluate image quality concerning respiratory motion blurring, sharpness measurements at the lung-liver interface were performed on the 3D radial FB images, using the slope of parametrized sigmoid functions⁴³. The analysis involved comparing images reconstructed under four methods: 1) without any motion compensation, 2) with PT-fNAV, 3) with PT-fNAV + denoising, and 4) with a motion-resolved reconstruction based on CS, guided by the same PT respiratory signal but without denoising. For the fourth method, end-expiratory slices were selected that were obtained after data binning into 4 respiratory states, as previously described⁴⁴. For each method, the same set of 20 coronal slices was analyzed. For each slice, sigmoid functions were fitted to 15 image segments perpendicular to the interface delineated with a manual selection and Bézier interpolation, and the mean sharpness per slice was reported. For all four methods, the mean sharpness and standard deviation across all slices and all volunteers were reported and statistical differences were assessed using paired Student's t-tests corrected for multiple comparisons, with $p<0.05$ considered significant.

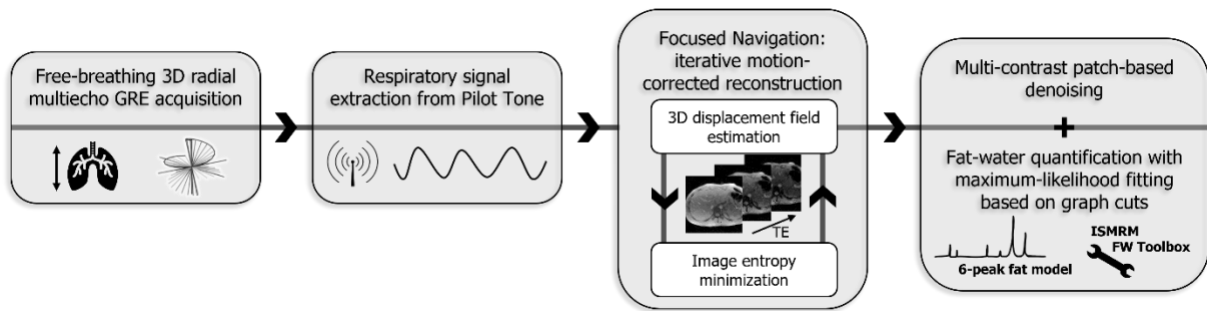


Figure 1 Acquisition, reconstruction, and post-processing steps for 3D free-breathing motion-corrected whole-liver fat-water quantification

Whole-liver data is collected during free-breathing with a 3D multiecho GRE sequence following a spiral phyllotaxis readout trajectory. The coil-integrated Pilot Tone navigator allows the retrospective monitoring of the chest position via the extraction of a 1D respiratory signal trace. This extracted respiratory signal is used to guide fNAV for motion-corrected image reconstruction. Then, multiecho imaging volumes are post-processed with patch-based denoising, and FF and $R2^*$ maps are generated using maximum-likelihood fitting and a reference 6-peak fat model.

2.3. Fat fraction and $R2^*$ quantification and analysis

The denoised PT-fNAV multiecho volumes were selected for fat fraction and $R2^*$ quantification. A maximum-likelihood algorithm based on graph cuts^{45,46} was used to quantify FF, B_0 and $R2^*$ and to obtain fat-only and water-only images. Fitting parameters included: a range of [-350;350] Hz for B_0 map estimation, a range of [0;100] Hz for $R2^*$ estimation with a single $T2^*$ decay component, $n=50$ graph cuts iterations, and a regularization term $\lambda=0.05$. A 6-peak liver fat spectral model⁴⁷ was used as input. An automatically generated background mask was placed on the denoised volumes, to accelerate the computation of the separated images and maps with the fitting algorithm. To provide reference fat-water images and maps, the 3D Cartesian BH multiecho images were reconstructed at the scanner and then post-processed using the same parameters. To account for the relatively large RF excitation angle ($\alpha=12^\circ$) a $T1$ bias correction⁴⁸ was performed on the FF maps (**Supporting Information S1**) following the methodology of Yang et al.⁴⁹

The fat-only and water-only images were qualitatively compared in terms of apparent species separation and contrast to the corresponding images obtained with the 3D Cartesian BH and the 2D 2-point Dixon VIBE BH scans. For quantitative comparisons, the FF and R2* maps produced from 3D radial FB and 3D Cartesian BH scans were assessed via ROI-based analyses. Note that with only 2 echoes, Dixon VIBE protocol cannot produce reliable parametric maps, therefore was not included in the comparison. An experienced abdominal radiologist (NVV) drew ROIs in three liver segments on the 2D MRQuantif BH images. From these, the MRQuantif software provided one mean FF and one mean R2* value per ROI (but no full parametric map, see **Supporting Information S2**). Then, the same ROIs were used to analyze the maps obtained from the 3D datasets. Maps exhibiting large and/or abrupt deviations towards extreme values (see **Supporting Information S3**) were reported as corrupted and discarded from the analysis when they occurred. Bland-Altman analyses and paired Student's t-test were performed to the precision and bias of the proposed 3D radial FB maps compared to the 3D Cartesian BH protocol and the MRQuantif measurements.

RESULTS

3.1. Validation of PT-fNAV for respiratory motion correction of 3D radial ME-GRE free-breathing data

In all volunteers, the respiratory signal curves extracted from the PT signals compared well with amplitude variations recorded by the respiration sensor (**Figure 2B**). The average image reconstruction time was 37min (PT-fNAV, with a range of [14-62]min), 48min (with added patch-based denoising, with a range of [15-73]min), 6.4h (motion-resolved, with a range of [4.9-14.5]h). PT-fNAV, both with and without denoising, improved image quality with

minimized motion-induced blurring at the lung-liver interface (**Figure 2A**, yellow arrows) and at the location of hepatic veins (**Figure 2A**, white arrows) in comparison to un-corrected images. Motion-resolved images, without denoising, appeared noisier across the whole FOV than PT-fNAV reconstructions without denoising (**Figure 2A**). Notably, the hepatic veins were more visible with PT-fNAV without denoising than with the CS-based reconstruction (**Figure 2A**, white arrows). Across the volunteer cohort, the average and standard deviation of the sharpness at the lung-liver interface was (0.155 ± 0.105) without motion compensation, (0.693 ± 0.104) with PT-fNAV, (0.741 ± 0.149) with PT-fNAV + denoising and (0.821 ± 0.175) with the motion-resolved reconstruction. While all three reconstruction methods showed a significant improvement in lung-liver interface sharpness ($p < 0.01$) compared to the non-compensated reconstruction, no significant differences in sharpness were found between any of the three techniques (PT-fNAV vs PT-fNAV + denoising: $p = 0.41$, PT-fNAV vs PT motion-resolved: $p = 0.36$, PT-fNAV + denoising vs PT motion-resolved: $p = 0.53$). While the end-expiratory motion-resolved images scored higher in sharpness, they displayed higher intra- and inter-volunteer variability (**Figure 2C**). It is to be noted that inter-volunteer variability followed a similar order across the techniques (e.g., in **Figure 2C**, V6 consistently scored the lowest).

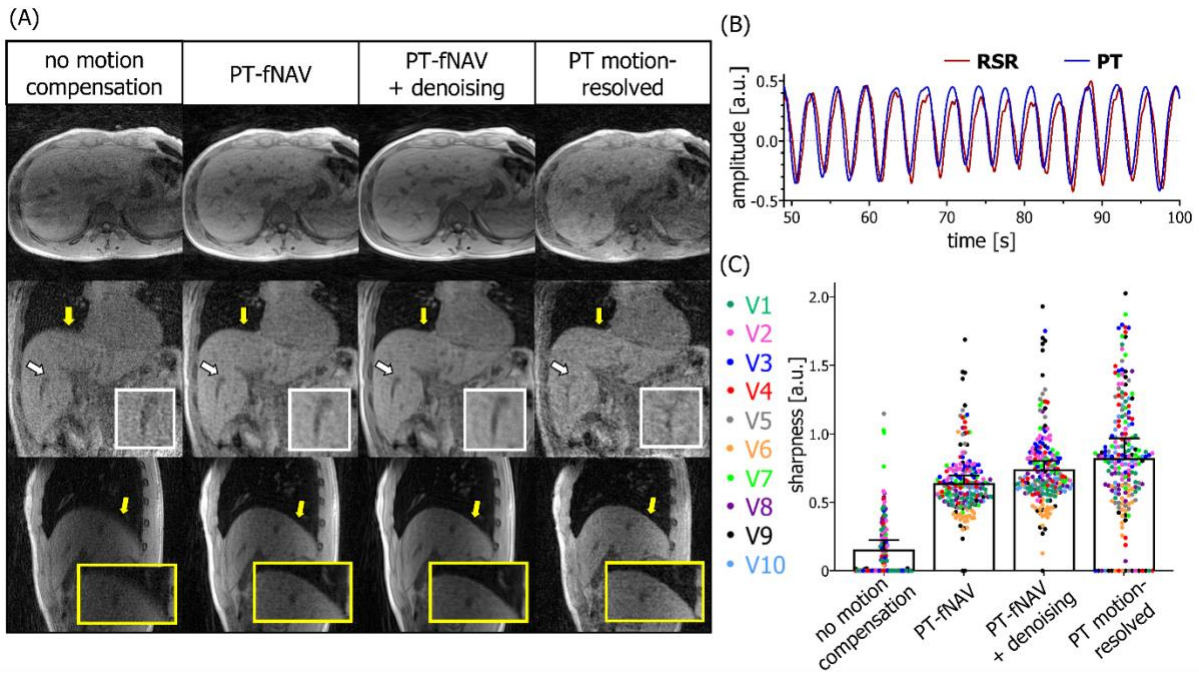


Figure 2 Different types of PT-driven respiratory motion compensation on 3D radial free-breathing multiecho data

(A) Image reconstructions of the 3D radial data collected at the first TE without motion compensation (simple gridding procedure with coil sensitivity estimation), with the PT-fNAV reconstruction (with and without denoising) and the motion-resolved CS reconstruction are shown in one volunteer. The resolution of details such as hepatic veins (white arrows) was improved with PT-fNAV, even without denoising, compared to the CS reconstruction (B) The corresponding Pilot Tone respiratory signal trace is shown next to the amplitude deviations measured by the respiratory sensor (RSR). (C) Sharpness measurements at the lung-liver interface for the 4 reconstruction techniques are shown for all $n=10$ volunteers (one color per volunteer, one dot per slice). Bars indicate the mean and standard deviation of the sharpness obtained in each reconstruction technique.

3.2. Fat-water separation and parametric quantification

In this section, we consider the fat-water separation and parametric quantification results obtained using the PT-fNAV + denoising reconstruction, which markedly improved image quality by effectively reducing motion artifacts in the water-fat images, the FF maps, and the $R2^*$ maps. No fat-water swaps were observed indicating a robust separation of chemical species (Figure 3). The water-only images obtained with the 3D radial FB scans displayed higher contrast between the hepatic vessels and the liver tissue than the images from 3D

Cartesian BH scans, thus comparing better to the 2D Cartesian VIBE images, which are characterized by lower fluid signal intensities in the hepatic veins.

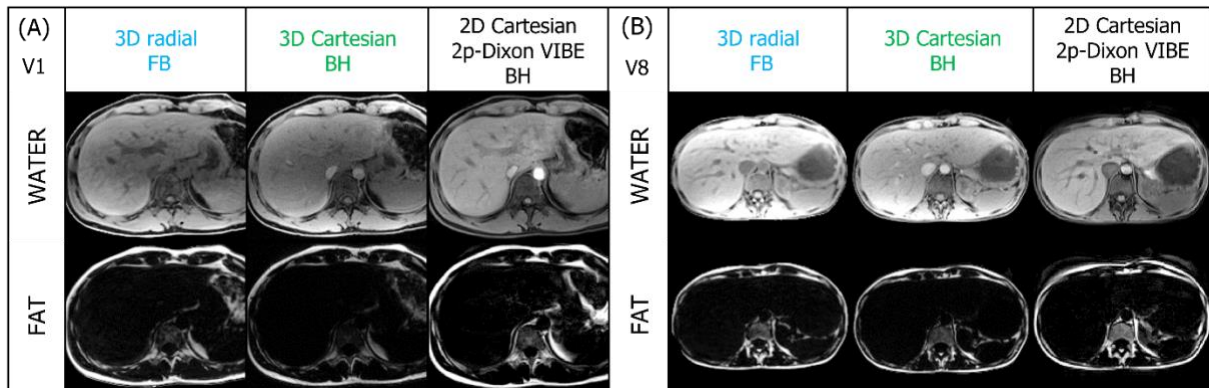


Figure 3 Fat-water separation with 3D radial FB, 3D Cartesian BH, and 2D Cartesian BH sequences in 2 volunteers

The water-only and fat-only images obtained with the 3D radial multiecho free-breathing sequence are compared to a 3D Cartesian breath-hold sequence with similar acquisition parameters. The first two columns of panels (A) and (B) (showing volunteers V1 and V8, respectively) show separated images obtained by fitting the reconstructed 8-echo datasets with a maximum-likelihood fitting routine based on graph cuts, using a spectral model of fat with 6 peaks. A second comparison is provided in the third column of each panel, in which water-fat separated images obtained with a routine 2-point 2D Cartesian VIBE BH sequence are displayed.

Throughout the volunteer cohort, out of the 80 slices collected with the 3D Cartesian BH scan, 4 FF maps and 15 R2* maps were reported as corrupted and discarded from quantitative analyses. It is to be noted that among the corrupted R2* maps, 60% occurred on a slice at the extremity of the 3D slab. No corrupted maps were reported within the 3D radial FB maps (see also **Supporting Information S3**).

In all other slices, FF maps from 3D radial data visually compared well with their 3D Cartesian counterparts (**Figure 4A**). The FF values estimated outside of the liver parenchyma were within the expected ranges for healthy adults (e.g., FF of 90-100% in the sub-cutaneous fat) for all sets of 3D maps. Hepatic ROI-based analyses showed a bias of +0.7% in fat fraction with limits of agreements (LOA) at [-2.5; 4.0]% between the proposed 3D radial FB maps and

the 3D Cartesian BH maps (**Figure 4C**), and the paired Student's t-test revealed a significant difference ($p < 0.01$) between the two measurement techniques. Differences were mostly driven by one volunteer for which higher ($>5\%$) fractions with high variability between slices and ROIs were detected (**Figure 4C**, V4). The comparison to FF measurements provided by the MRQuantif software showed a bias of -0.9% with LOA $[-1.7; 0.1]\%$ for the 3D Cartesian maps and a bias of -0.2% with LOA $[-1.1; 0.6]\%$ for the 3D radial maps (**Figure 4E**). Detailed FF measurements are provided in table format in **Supporting Information S4**.

While the $R2^*$ values estimated with both 3D protocols ranged within the normal values at $1.5T^{50}$, the global appearance of the maps differed more substantially (**Figure 4B**). Maps from the 3D radial FB scans showed overall larger distributions in $R2^*$ across the different liver segments, with in some cases high values estimated at the posterior edge of the lobe, due to magnetic susceptibility effects close to the air-filled lungs (**Figure 4B**, arrow). In comparison, $R2^*$ maps from Cartesian scans displayed more homogeneous values across the organ. Bland-Altman analyses showed a bias of $3.2s^{-1}$ with LOA $[-12; 19]\%$ between $R2^*$ estimated from 3D Cartesian BH and 3D radial FB scans (**Figure 4D**). With respect to MRQuantif values (**Figure 4F**), the $R2^*$ bias from 3D Cartesian BH scans was $0.2s^{-1}$ with LOA $[17; 17]s^{-1}$. 3D radial $R2^*$ maps showed a larger bias with MRQuantif at $0.6s^{-1}$, but with tighter limits of agreement at $[-7.9; 6.7]s^{-1}$. The FF values obtained with the graphcut algorithm in the evaluated ROIs were statistically similar, both when comparing the 3D radial FB and the 3D Cartesian BH to MRQuantif values and between themselves.

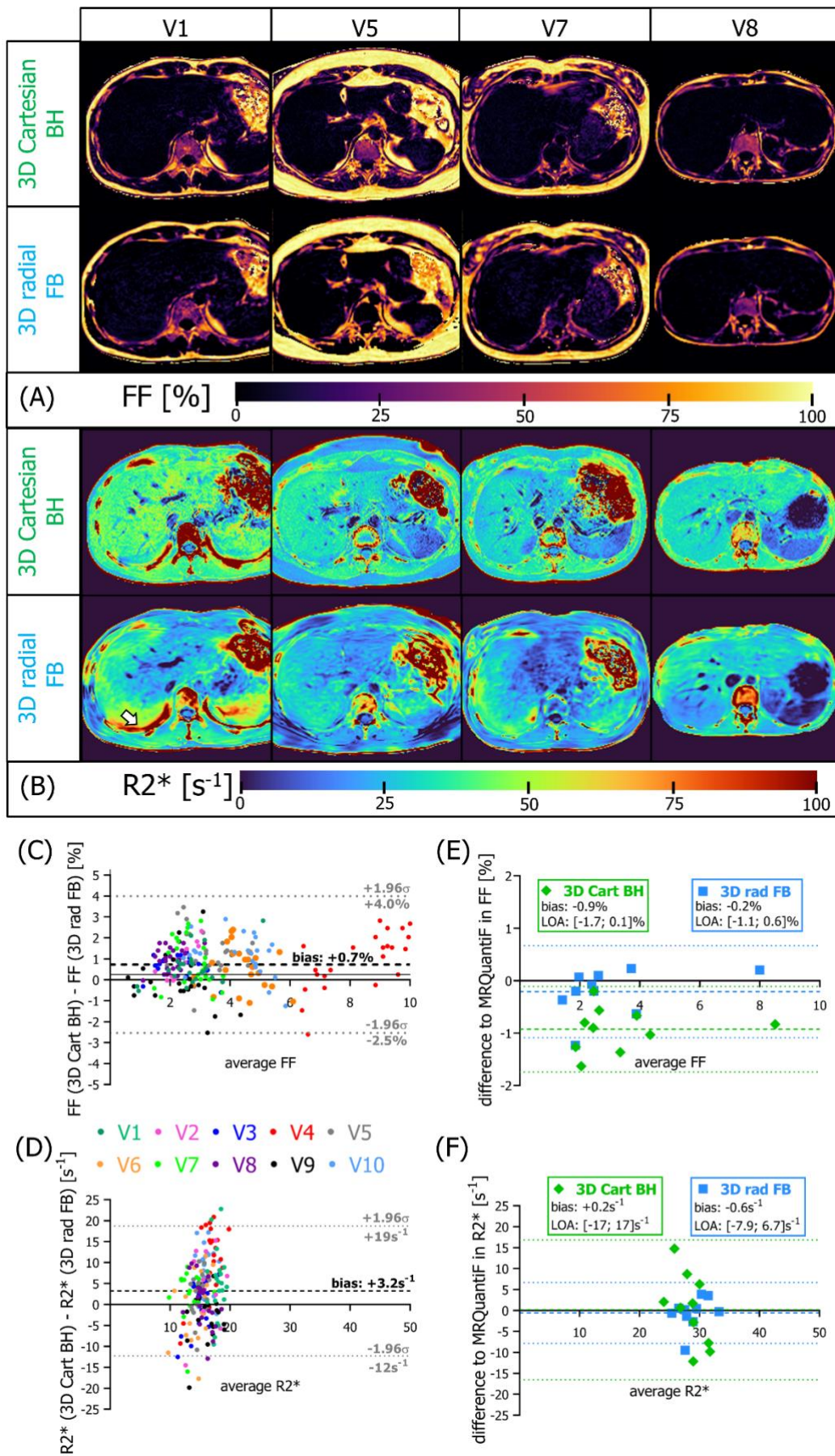


Figure 4 Fat and R2* parametric maps and Bland-Altman analyses in volunteers

Transversal fat fraction (A) and R2* (B) maps obtained with the graph cut algorithm from the proposed 3D radial free-breathing acquisition and the reference 3D Cartesian breath-hold scan in 4 volunteers (from left to right: V1, V5, V7, V8). The bias and limits of agreement (LOA) of the proposed radial technique with respect to the 3D Cartesian are reported for FF (C) and R2* (D). In (C) and (D), mean and standard deviation measurements were performed in 3 ROIs over a central slab (8 Cartesian slices, 20 radial slices) for each volunteer as indicated by the colour code. In (E) and (F), the bias and LOA of both 3D techniques with respect to the 2D MRQuantIF BH measurements are reported for FF and R2* for all 10 volunteers. The mean FF (E) and R2* (F) values measured over all ROIs and slices in the 3D maps are compared to the mean values provided by the MRQuantIF software.

DISCUSSION

With the proposed approach, data to construct whole liver maps of FF and R2* was acquired in a scan time under 3min, thus clinically feasible⁵¹, while providing additional echo sampling and a 3D isotropic resolution with a considerable improvement in ease-of-use for the examiner. A comprehensive comparison of four different image reconstruction techniques for whole-liver free-breathing imaging data, and a comparison with reference breath hold scans, revealed that the motion-corrected PT-fNAV reconstruction allowed for noise reduction and preserved edge sharpness at the lung-liver interface, even without performing additional denoising and compared with a compressed sensing-based motion-resolved approach. To our knowledge, this is the first use of fNAV and Pilot Tone for quantitative and structural whole-liver MRI.

Fat quantification using the proposed 3D radial approach agreed with values from reference scans. The calculated biases in FF quantification were in general below 1%, which is lower than the typically observed sensitivity range of CSE-MRI. These findings show that the proposed technique provides coherent 3D mapping volumes, with no mismatches between adjacent slices that can be reported with methods that use slice-encoding. The effect of susceptibility on R2* quantification⁵² was observed both in end-inspiration BH Cartesian

acquisitions with large air-filled regions and more so in 3D radial FB, at locations of expected higher motion amplitudes. This is in line with prior investigations which reported respiratory-induced $R2^*$ aliasing^{11,28,29}, and suggests potential residual motion artifacts and a higher sensitivity to motion compared to FF maps.

This work addresses the need for whole-liver fat quantification during free-breathing, thus enabling 3D monitoring of potentially inhomogeneous steatosis, even in patients with limited pulmonary capacities. Additionally, the integration of the sequence into the clinical practice is simplified due to the single-click approach of the 3D FB scan. The use of Pilot Tone technology to monitor liver motion may benefit low SNR 3D radial sequences instead of traditional self-gating^{21,30} or similarity-driven binning algorithms⁵³. It opens new avenues in trajectory design that more uniformly covers k-space and could improve robustness to gradient imperfections⁵⁴. In addition, PT technology combined with free-breathing acquisitions will enable the translation of fat quantification methods that require a magnetization steady-state⁵⁵.

Still, the requirement for clinical adaptation of free-breathing quantification techniques is a rapid online image reconstruction. By opting for motion correction with fNAV and image-based parametric mapping, the computational burden is heavily reduced compared to CS-based reconstructions. Additionally, the choice of monopolar readouts avoid the need for gradient corrections^{56–58} in the reconstruction pipeline. Furthermore, the denoising step did not significantly impact the overall results and could therefore be omitted from the reconstruction. With the emergence of open-source workflows^{59,60} for image reconstruction, our proposed approach could be implemented on an MR scanner.

A comprehensive validation in fatty livers of available FB techniques, including comparisons between 3D radial and stack-of-stars trajectories that are more common for

abdominal imaging^{21,28,31–33}, should be performed in future work as to complete the validation⁶³. Nevertheless, this study performed in healthy subjects at 1.5T demonstrates the feasibility of obtaining accurate parametric maps of hepatic fat from FB scans with relatively accessible tools such as Pilot Tone for retrospective motion monitoring and an open-source fitting algorithm⁴⁶.

CONCLUSION

In conclusion, this study validated a 3D radial FB pipeline with PT-fNAV motion correction for accurate fat quantification of the whole liver in under 3 minutes of scan time, with a user-friendly sequence. This approach presents a promising alternative to conventional 2D and 3D BH scans for populations with reduced respiratory capabilities.

ACKNOWLEDGMENTS

We acknowledge the use of the ISMRM Fat–Water Toolbox (<http://ismrm.org/workshops/FatWater12/data.htm>) for some of the results shown in this article.

This study was supported by funding received from the Swiss National Science Foundation (grants PCEFP2_194296 and PZ00P3_167871 to J.A.M.B., grant PZ00P3_202140 to C.W.R., grants 320030B_201292 and 320030_173129 to M.S.), the University of Lausanne Bourse Pro-Femmes (J.A.M.B.), the Emma Muschamp Foundation (J.A.M.B.) and the Swiss Heart Foundation (grant FF18054 to J.A.M.B.).

CONFLICT OF INTEREST STATEMENT

Mario Bacher and Peter Speier are employees of Siemens Healthcare AG. Matthias Stuber receives non-monetary research support from Siemens Healthineers.

DATA AVAILABILITY STATEMENT

All anonymized volunteer datasets (n=10), consisting of (1) the 3D radial FB raw data files, (2) the raw Pilot Tone signals and the extracted respiratory signals, and (3) the reference images obtained from the 3D Cartesian BH and 2D 2p-Dixon VIBE sequences are available publicly at the following repository: <https://zenodo.org/records/8338128>.

REFERENCES

1. Younossi ZM, Koenig AB, Abdelatif D, Fazel Y, Henry L, Wymer M. Global epidemiology of nonalcoholic fatty liver disease—Meta-analytic assessment of prevalence, incidence, and outcomes. *Hepatology*. 2016;64(1):73-84. doi:10.1002/hep.28431
2. Bray GA. Medical Consequences of Obesity. *J Clin Endocrinol Metab*. 2004;89(6):2583-2589. doi:10.1210/jc.2004-0535
3. Reeder SB, Wen Z, Yu H, et al. Multicoil Dixon chemical species separation with an iterative least-squares estimation method. *Magn Reson Med*. 2004;51(1):35-45. doi:10.1002/mrm.10675
4. Yu H, McKenzie CA, Shimakawa A, et al. Multiecho reconstruction for simultaneous water-fat decomposition and T2* estimation. *J Magn Reson Imaging*. 2007;26(4):1153-1161. doi:10.1002/jmri.21090
5. Bray TJ, Chouhan MD, Punwani S, Bainbridge A, Hall-Craggs MA. Fat fraction mapping using magnetic resonance imaging: insight into pathophysiology. *Br J Radiol*. 2018;91(1089):20170344. doi:10.1259/bjr.20170344
6. Idilman IS, Aniktar H, Idilman R, et al. Hepatic Steatosis: Quantification by Proton Density Fat Fraction with MR Imaging versus Liver Biopsy. *Radiology*. 2013;267(3):767-775. doi:10.1148/radiol.13121360
7. Kühn JP, Hernando D, Muñoz del Rio A, et al. Effect of Multipeak Spectral Modeling of Fat for Liver Iron and Fat Quantification: Correlation of Biopsy with MR Imaging Results. *Radiology*. 2012;265(1):133-142. doi:10.1148/radiol.12112520
8. Gu J, Liu S, Du S, et al. Diagnostic value of MRI-PDFF for hepatic steatosis in patients with non-alcoholic fatty liver disease: a meta-analysis. *Eur Radiol*. 2019;29(7):3564-3573. doi:10.1007/s00330-019-06072-4
9. Nassir F, Rector RS, Hammoud GM, Ibdah JA. Pathogenesis and Prevention of Hepatic Steatosis. *Gastroenterol Hepatol*. 2015;11(3):167-175.
10. Neeland IJ, Marso SP, Ayers CR, et al. Effects of liraglutide on visceral and ectopic fat in adults with overweight and obesity at high cardiovascular risk: a randomised, double-blind, placebo-controlled, clinical trial. *Lancet Diabetes Endocrinol*. 2021;9(9):595-605. doi:10.1016/S2213-8587(21)00179-0
11. Starekova J, Hernando D, Pickhardt PJ, Reeder SB. Quantification of Liver Fat Content with CT and MRI: State of the Art. *Radiology*. 2021;301(2):250-262. doi:10.1148/radiol.2021204288
12. Reeder SB, Robson PM, Yu H, et al. Quantification of hepatic steatosis with MRI: The effects of accurate fat spectral modeling. *J Magn Reson Imaging*. 2009;29(6):1332-1339. doi:10.1002/jmri.21751
13. Hu F, Yang R, Huang Z, et al. 3D Multi-Echo Dixon technique for simultaneous assessment of liver steatosis and iron overload in patients with chronic liver diseases: a feasibility study. *Quant Imaging Med Surg*. 2019;9(6):1014-1024. doi:10.21037/qims.2019.05.20
14. Fernandez M, Lokan J, Leung C, Grigg A. A critical evaluation of the role of iron overload in fatty liver disease. *J Gastroenterol Hepatol*. 2022;37(10):1873-1883. doi:10.1111/jgh.15971
15. Qayyum A, Nystrom M, Noworolski S, Chu P, Mohanty A, Merriman R. MRI Steatosis Grading: Development and Initial Validation of a Color Mapping System. *AJR Am J Roentgenol*. 2012;198:582-588. doi:10.2214/AJR.11.6729

16. Vu KN, Gilbert G, Chalut M, Chagnon M, Chartrand G, Tang A. MRI-determined liver proton density fat fraction, with MRS validation: Comparison of regions of interest sampling methods in patients with type 2 diabetes. *J Magn Reson Imaging*. 2016;43(5):1090-1099. doi:10.1002/jmri.25083
17. Rofsky NM, Lee VS, Laub G, et al. Abdominal MR Imaging with a Volumetric Interpolated Breath-hold Examination. *Radiology*. 1999;212(3):876-884. doi:10.1148/radiology.212.3.r99se34876
18. Zhong X, Nickel MD, Kannengiesser SAR, Dale BM, Kiefer B, Bashir MR. Liver fat quantification using a multi-step adaptive fitting approach with multi-echo GRE imaging. *Magn Reson Med*. 2014;72(5):1353-1365. doi:10.1002/mrm.25054
19. Henninger B, Zoller H, Kannengiesser S, Zhong X, Jaschke W, Kremser C. 3D Multiecho Dixon for the Evaluation of Hepatic Iron and Fat in a Clinical Setting. *J Magn Reson Imaging*. 2017;46(3):793-800. doi:10.1002/jmri.25630
20. Vietti Violi N, Hilbert T, Bastiaansen JAM, et al. Patient respiratory-triggered quantitative T2 mapping in the pancreas. *J Magn Reson Imaging*. 2019;50(2):410-416. doi:10.1002/jmri.26612
21. Armstrong T, Zhong X, Shih SF, et al. Free-breathing 3D stack-of-radial MRI quantification of liver fat and R2* in adults with fatty liver disease. *Magn Reson Imaging*. 2022;85:141-152. doi:10.1016/j.mri.2021.10.016
22. Gilligan LA, Dillman JR, Tkach JA, Trout AT. Comparison of navigator-gated and breath-held image acquisition techniques for multi-echo quantitative dixon imaging of the liver in children and young adults. *Abdom Radiol*. 2019;44(6):2172-2181. doi:10.1007/s00261-019-01960-1
23. Starekova J, Zhao R, Colgan TJ, et al. Improved free-breathing liver fat and iron quantification using a 2D chemical shift-encoded MRI with flip angle modulation and motion-corrected averaging. *Eur Radiol*. 2022;32(8):5458-5467. doi:10.1007/s00330-022-08682-x
24. Feng L. Golden-Angle Radial MRI: Basics, Advances, and Applications. *J Magn Reson Imaging*. 2022;56(1):45-62. doi:10.1002/jmri.28187
25. Chandarana H, Feng L, Block TK, et al. Free-Breathing Contrast-Enhanced Multiphase MRI of the Liver Using a Combination of Compressed Sensing, Parallel Imaging, and Golden-Angle Radial Sampling. *Invest Radiol*. 2013;48(1):10.1097/RLI.0b013e318271869c. doi:10.1097/RLI.0b013e318271869c
26. Arboleda C, Aguirre-Reyes D, García MP, et al. Total liver fat quantification using three-dimensional respiratory self-navigated MRI sequence. *Magn Reson Med*. 2016;76(5):1400-1409. doi:10.1002/mrm.26028
27. Armstrong T, Dregely I, Stemmer A, et al. Free-breathing liver fat quantification using a multiecho 3D stack-of-radial technique. *Magn Reson Med*. 2018;79(1):370-382. doi:10.1002/mrm.26693
28. Zhong X, Armstrong T, Nickel MD, et al. Effect of respiratory motion on free-breathing 3D stack-of-radial liver relaxometry and improved quantification accuracy using self-gating. *Magn Reson Med*. 2020;83(6):1964-1978. doi:10.1002/mrm.28052
29. Schneider M, Benkert T, Solomon E, et al. Free-breathing fat and R2* quantification in the liver using a stack-of-stars multi-echo acquisition with respiratory-resolved model-based reconstruction. *Magn Reson Med*. 2020;84(5):2592-2605. doi:10.1002/mrm.28280
30. Zhong X, Hu HH, Armstrong T, et al. Free-Breathing Volumetric Liver and Proton Density Fat Fraction Quantification in Pediatric Patients Using Stack-of-Radial MRI With Self-

- Gating Motion Compensation. *J Magn Reson Imaging*. 2021;53(1):118-129. doi:10.1002/jmri.27205
31. Tan Z, Unterberg-Buchwald C, Blumenthal M, et al. Free-Breathing Liver Fat, R_2^* and B_0 Field Mapping Using Multi-Echo Radial FLASH and Regularized Model-Based Reconstruction. *IEEE Trans Med Imaging*. 2023;42(5):1374-1387. doi:10.1109/TMI.2022.3228075
 32. Armstrong T, Ly KV, Murthy S, et al. Free-breathing quantification of hepatic fat in healthy children and children with nonalcoholic fatty liver disease using a multi-echo 3-D stack-of-radial MRI technique. *Pediatr Radiol*. 2018;48(7):941-953. doi:10.1007/s00247-018-4127-7
 33. Armstrong T, Ly KV, Ghahremani S, Calkins KL, Wu HH. Free-breathing 3-D quantification of infant body composition and hepatic fat using a stack-of-radial magnetic resonance imaging technique. *Pediatr Radiol*. 2019;49(7):876-888. doi:10.1007/s00247-019-04384-7
 34. Roy CW, Heerfordt J, Piccini D, et al. Motion compensated whole-heart coronary cardiovascular magnetic resonance angiography using focused navigation (fNAV). *J Cardiovasc Magn Reson*. 2021;23(1):33. doi:10.1186/s12968-021-00717-4
 35. Atkinson D, Hill DLG, Stoye PNR, Summers PE, Keevil SF. Automatic correction of motion artifacts in magnetic resonance images using an entropy focus criterion. *IEEE Trans Med Imaging*. 1997;16(6):903-910. doi:10.1109/42.650886
 36. Cheng JY, Alley MT, Cunningham CH, Vasanaawala SS, Pauly JM, Lustig M. Nonrigid motion correction in 3D using autofocusing with localized linear translations. *Magn Reson Med*. 2012;68(6):1785-1797. doi:10.1002/mrm.24189
 37. Falcão MBL, Rossi GMC, Rutz T, et al. Focused navigation for respiratory–motion-corrected free-running radial 4D flow MRI. *Magn Reson Med*. 2023;90(1):117-132. doi:10.1002/mrm.29634
 38. Mackowiak ALC, Roy CW, Yerly J, et al. Motion-resolved fat-fraction mapping with whole-heart free-running multiecho GRE and pilot tone. *Magn Reson Med*. 2023;90(3):922-938. doi:10.1002/mrm.29680
 39. Vahle T, Bacher M, Rigie D, et al. Respiratory Motion Detection and Correction for MR Using the Pilot Tone: Applications for MR and Simultaneous PET/MR Exams. *Invest Radiol*. 2020;55(3):153-159. doi:10.1097/RLI.0000000000000619
 40. Piccini D, Littmann A, Nielles-Vallespin S, Zenge MO. Spiral phyllotaxis: The natural way to construct a 3D radial trajectory in MRI. *Magn Reson Med*. 2011;66(4):1049-1056. doi:10.1002/mrm.22898
 41. Falcão MBL, Di Sopra L, Ma L, et al. Pilot tone navigation for respiratory and cardiac motion-resolved free-running 5D flow MRI. *Magn Reson Med*. 2022;87(2):718-732. doi:10.1002/mrm.29023
 42. Bustin A, Lima da Cruz G, Jaubert O, Lopez K, Botnar RM, Prieto C. High-dimensionality undersampled patch-based reconstruction (HD-PROST) for accelerated multi-contrast MRI. *Magn Reson Med*. 2019;81(6):3705-3719. doi:10.1002/mrm.27694
 43. Ahmad R, Ding Y, Simonetti OP. Edge sharpness assessment by parametric modeling: Application to magnetic resonance imaging. *Concepts Magn Reson Part A*. 2015;44(3):138-149. doi:10.1002/cmr.a.21339
 44. Piccini D, Feng L, Bonanno G, et al. Four-dimensional respiratory motion-resolved whole heart coronary MR angiography. *Magn Reson Med*. 2017;77(4):1473-1484. doi:10.1002/mrm.26221

45. Hernando D, Kellman P, Haldar JP, Liang ZP. Robust water/fat separation in the presence of large field inhomogeneities using a graph cut algorithm. *Magn Reson Med*. 2010;63(1):79-90. doi:10.1002/mrm.22177
46. Hu HH, Börnert P, Hernando D, et al. ISMRM workshop on fat–water separation: Insights, applications and progress in MRI. *Magn Reson Med*. 2012;68(2):378-388. doi:10.1002/mrm.24369
47. Yu H, Shimakawa A, McKenzie CA, Brodsky E, Brittain JH, Reeder SB. Multiecho water-fat separation and simultaneous R estimation with multifrequency fat spectrum modeling. *Magn Reson Med*. 2008;60(5):1122-1134. doi:10.1002/mrm.21737
48. de Bazelaire CMJ, Duhamel GD, Rofsky NM, Alsop DC. MR Imaging Relaxation Times of Abdominal and Pelvic Tissues Measured in Vivo at 3.0 T: Preliminary Results. *Radiology*. 2004;230(3):652-659. doi:10.1148/radiol.2303021331
49. Yang IY, Cui Y, Wiens CN, Wade TP, Friesen-Waldner LJ, McKenzie CA. Fat fraction bias correction using T1 estimates and flip angle mapping. *J Magn Reson Imaging*. 2014;39(1):217-223. doi:10.1002/jmri.24126
50. Obrzut M, Atamaniuk V, Glaser KJ, et al. Value of liver iron concentration in healthy volunteers assessed by MRI. *Sci Rep*. 2020;10(1):17887. doi:10.1038/s41598-020-74968-z
51. Pooler BD, Hernando D, Reeder SB. Clinical Implementation of a Focused MRI Protocol for Hepatic Fat and Iron Quantification. *AJR Am J Roentgenol*. March 2019:1-6. doi:10.2214/AJR.18.20947
52. Obmann VC, Mertineit N, Marx C, et al. Liver MR relaxometry at 3T – segmental normal T1 and T2* values in patients without focal or diffuse liver disease and in patients with increased liver fat and elevated liver stiffness. *Sci Rep*. 2019;9(1):8106. doi:10.1038/s41598-019-44377-y
53. Heerfordt J, Whitehead KK, Bastiaansen JAM, et al. Similarity-driven multi-dimensional binning algorithm (SIMBA) for free-running motion-suppressed whole-heart MRA. *Magn Reson Med*. February 2021. doi:10.1002/mrm.28713
54. Bieri O, Pusterla O, Bauman G. Free-breathing half-radial dual-echo balanced steady-state free precession thoracic imaging with wobbling Archimedean spiral pole trajectories. *Z Für Med Phys*. 2023;33(2):220-229. doi:10.1016/j.zemedi.2022.01.003
55. Rossi GMC, Mackowiak ALC, Açıkgöz BC, et al. SPARCQ: A new approach for fat fraction mapping using asymmetries in the phase-cycled balanced SSFP signal profile. *Magn Reson Med*. 2023;90(6):2348-2361. doi:10.1002/mrm.29813
56. Yu H, Shimakawa A, McKenzie CA, et al. Phase and amplitude correction for multi-echo water–fat separation with bipolar acquisitions. *J Magn Reson Imaging*. 2010;31(5):1264-1271. doi:10.1002/jmri.22111
57. Rosenzweig S, Holme HCM, Uecker M. Simple auto-calibrated gradient delay estimation from few spokes using Radial Intersections (RING). *Magn Reson Med*. 2019;81(3):1898-1906. doi:10.1002/mrm.27506
58. Daude P, Troalen T, Mackowiak A, et al. Quantitative Magnetic Resonance Imaging of the epicardial adipose tissue with free-running cardiac Dixon. *Arch Cardiovasc Dis Suppl*. 2023;15(2):238. doi:10.1016/j.acvdsp.2023.03.130
59. Hansen MS, Sørensen TS. Gadgetron: An open source framework for medical image reconstruction. *Magn Reson Med*. 2013;69(6):1768-1776. doi:10.1002/mrm.24389
60. Veldmann M, Ehses P, Chow K, Nielsen JF, Zaitsev M, Stöcker T. Open-source MR imaging and reconstruction workflow. *Magn Reson Med*. 2022;88(6):2395-2407. doi:10.1002/mrm.29384

SUPPORTING INFORMATION

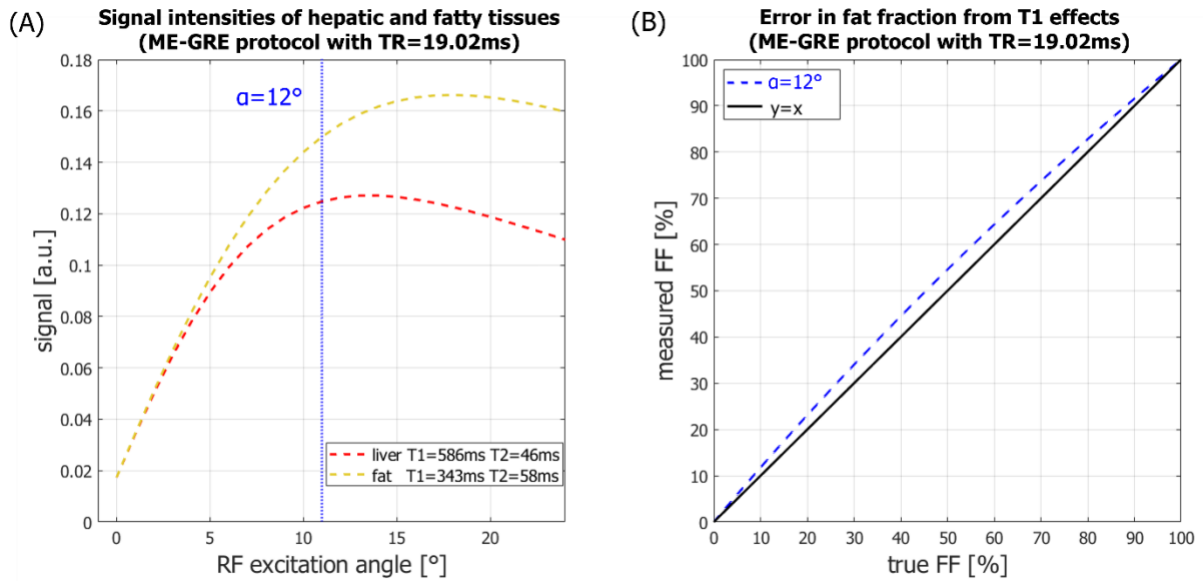
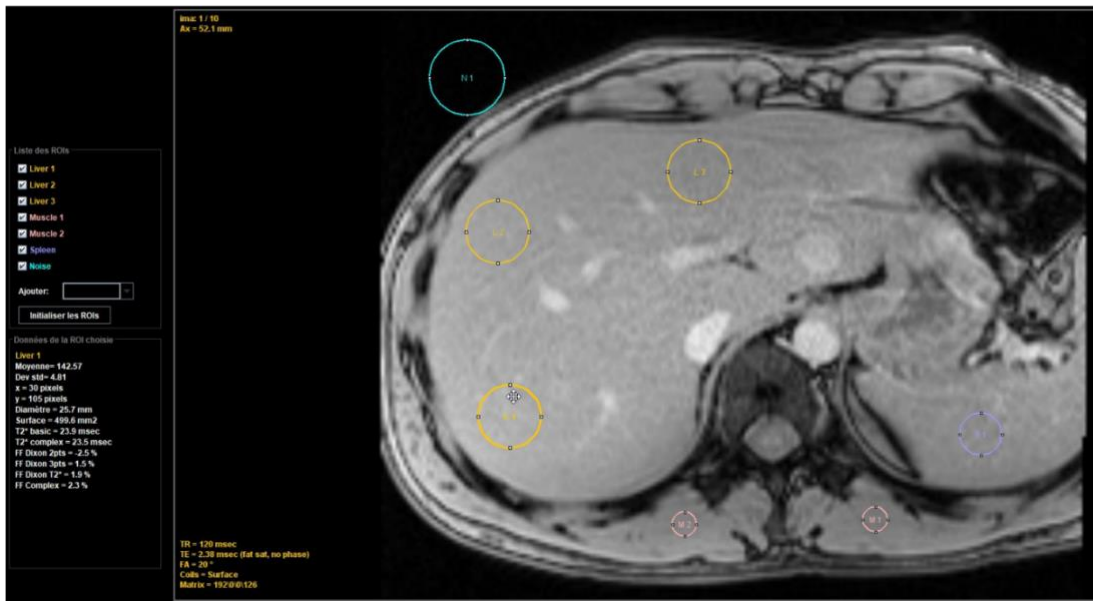


Figure S1 T1 bias correction curves

Due to the relatively short T1 of fat in comparison to water-based tissues, the accelerated T1 recovery process amplifies the signal intensity of fat, resulting in apparent increases in FF. This effect is both TR- and flip-angle-dependent. To mitigate T1 bias, a common method involves low flip angle ($\alpha < 5^\circ$) acquisitions; however, this can lead to substantial SNR loss for acquisitions with numerous echoes and long TR, as employed in this work. In our study, we used a flip angle of $\alpha = 12^\circ$ for the ME-GRE scans and the method validated by Yang et al.⁴⁹ to correct for T1-induced errors in fat fraction estimations. Based on relaxometry constants reported in the literature by Bazelaire et al.⁴⁸ for normal tissues at 1.5T, a TR-adjusted correction factor of $\kappa = 1.2021$ was computed and used to correct the FF estimations of the ISMRM Fat-Water Toolbox⁴⁶. The maximal deviation from true fat fraction (B) with the proposed sequence was 4.6% for FF=47.7%.

(A)



(B)

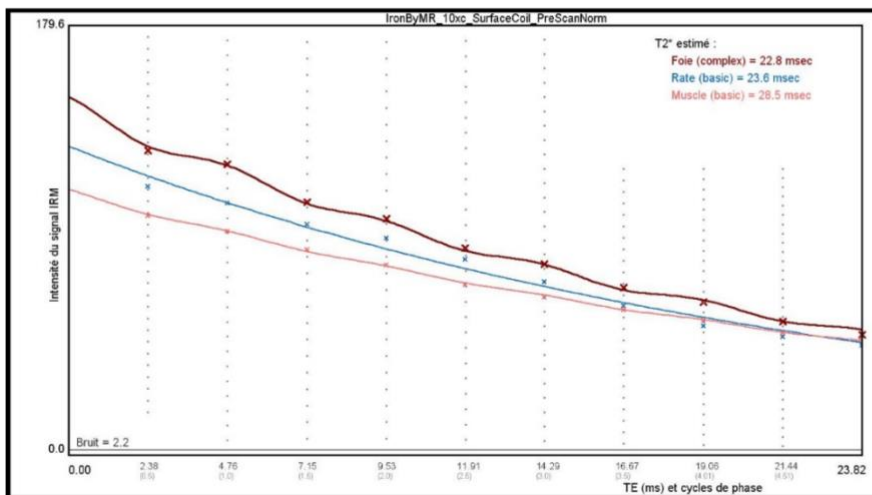


Figure S2 Fat and iron quantification with MRQuantif software

MRQuantif (<https://imageded.univ-rennes1.fr/en/mrquantif/overview>) is a free software developed at the University of Rennes, France. MRQuantif is routinely used by clinicians at our institution for hepatic fat and iron quantification. The MRI protocol used in our study follows the recommended guidelines provided by the developers. After imaging with the 10-echo GRE sequence, the sources images are reconstructed at the scanner in DICOM format. The interface of the MRQuantif processing software on a PACS workstation is shown in (A), with the three liver ROI drawn in yellow. Quantification results for the selected ROI appear in the bottom left panel. T2* decay curves are also provided for visualization (B). For fat quantification, note that no T1 bias correction is performed on the FF estimates as the MRQuantif protocol uses a long repetition time (TR=120ms) which minimizes T1 bias despite the high flip angle of 20°.

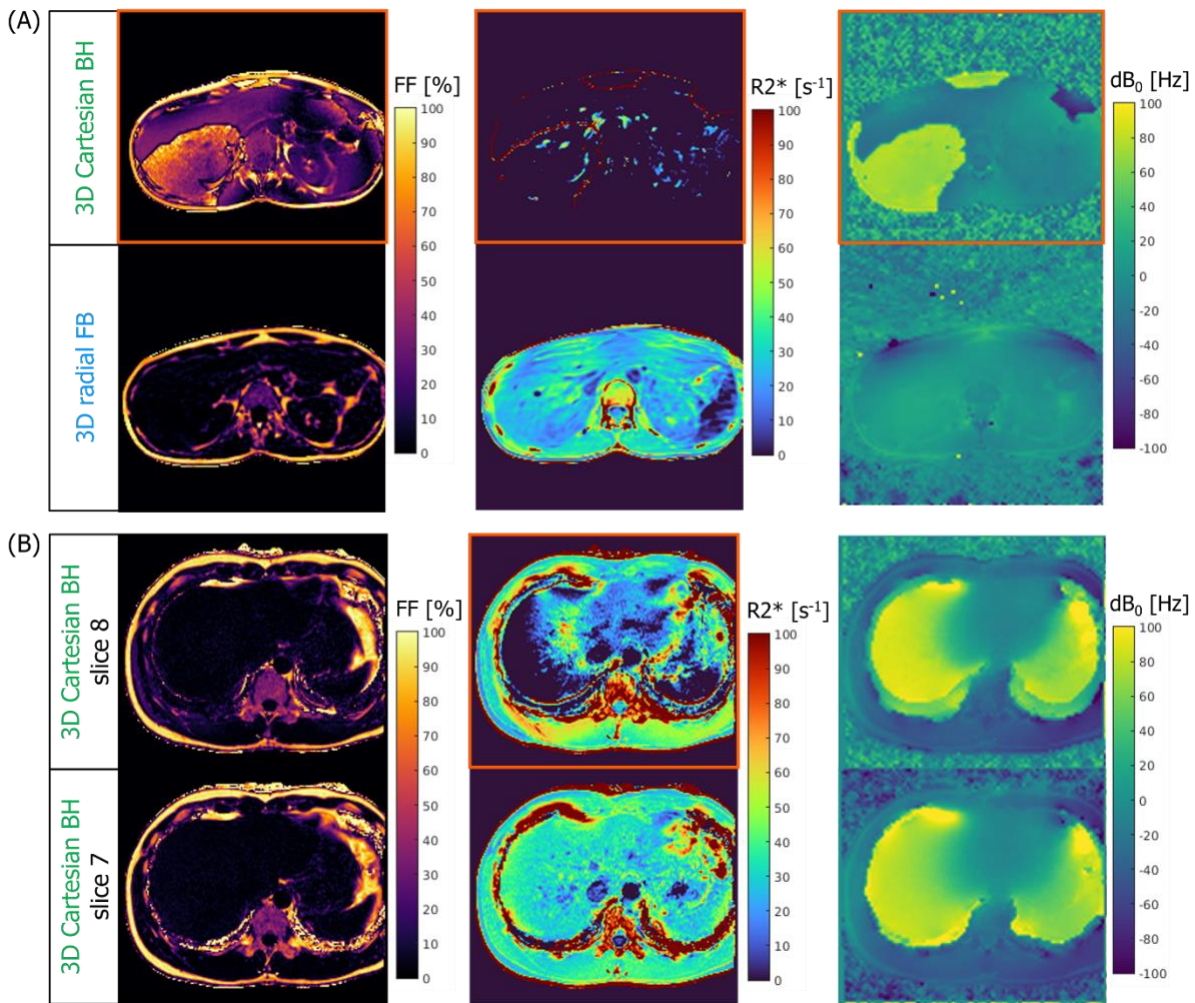


Figure S3 Examples of corrupted FF and $R2^*$ maps obtained with a maximum-likelihood fitting routine

Fat fraction (FF), $R2^*$ and B_0 field maps obtained with a maximum-likelihood fitting routine based on graph cuts are displayed for two volunteers. Corrupted maps are highlighted by an orange frame. In panel (A), both the FF and $R2^*$ map obtained with the 3D Cartesian acquisition are corrupted, with over-estimations in FF and null $R2^*$ values found over the entire FOV. The pattern of the mis-estimations follows a patchy appearance observed in the B_0 field map, indicating the failure to estimate fat and $R2^*$ is the result of a mis-estimation of the B_0 field map. For reference, the corresponding (non-corrupted) maps obtained with the 3D radial FB acquisition are displayed in the second row of panel (A). In panel (B), one slice (slice 8, first row) of the $R2^*$ map obtained from the Cartesian BH acquisition showed large deviations from the values estimated in the adjacent slice (slice 7, second row), notably with null values found in the parenchyma. In this case, the FF map was not corrupted and the B_0 field map matched with that of the adjacent slice. In this study, all slices for which at least one map was identified as corrupted were discarded from the quantitative analyses reported.

	3D radial FB						3D Cartesian BH						2D MRQuantif					
	ROI 1		ROI 2		ROI 3		ROI 1		ROI 2		ROI 3		ROI 1		ROI 2		ROI 3	
	mean ± std	n	mean ± std	n	mean ± std	n	mean ± std	n	mean ± std	n	mean ± std	n	mean	n	mean	n	mean	n
V1	2.9±0.6	4660	2.2±0.5	4024	2.2±0.6	4078	3.2±0.6	1979	3.0±0.6	1986	2.6±0.6	1931	2.3	142	3.0	129	1.8	110
V2	1.8±0.2	4248	2.0±0.2	3652	2.0±0.3	2305	3.5±0.9	701	3.2±0.9	740	2.0±0.5	555	2.0	130	2.0	114	2.0	94
V3	2.5±1.0	4220	2.0±0.4	5617	1.4±0.3	3387	2.7±0.8	2104	2.9±0.5	2815	2.1±0.3	1965	2.3	127	2.0	94	1.0	96
V4	8.2±0.6	3867	8.1±1.2	4214	7.4±0.6	3909	10.6±0.9	1996	9.8±1.1	1734	6.4±1.0	2078	8.9	119	8.3	109	7.1	96
V5	2.6±0.7	3731	3.4±0.4	5337	1.7±1.3	4066	3.7±0.6	1600	4.5±0.9	2108	3.9±1.0	2155	2.8	128	3.5	145	1.7	155
V6	4.6±1.1	4679	3.4±0.9	4881	4.6±0.8	3781	4.3±0.9	2269	4.2±1.0	2007	4.2±1.1	1091	3.6	146	3.3	129	3.8	123
V7	2.7±1.0	6097	1.8±0.8	5037	2.9±0.9	6033	2.7±0.9	2931	2.8±1.1	2779	3.1±0.5	2714	2.0	130	1.7	145	0.0	156
V8	1.1±0.4	5574	1.6±0.3	4910	2.1±0.2	4832	2.6±0.4	2195	2.2±0.7	1754	2.7±0.7	1317	1.1	147	1.4	133	1.2	139
V9	4.1±1.3	4320	2.5±1.0	4184	1.1±0.4	4333	3.1±1.3	2054	2.0±0.8	1939	2.6±1.7	2175	2.2	137	3.0	129	1.9	130
V10	4.7±1.0	5593	4.1±0.9	4506	2.0±0.4	6342	5.4±0.4	3146	5.5±0.6	2570	3.7±0.9	3011	4.6	125	4.2	109	2.7	106

Table S4 Table of parametric FF measurements

For each measurement technique (3D radial FB, 3D Cartesian BH, 2D MRQuantif) the mean (and standard deviation, when provided) fat fraction and the number of voxels per region of interest over the whole measurement volume (respectively 20,8, and 1 slice(s) for 3D radial FB, 3D Cartesian BH and 2D MRQuantif) are reported.